
Article:
Shen, X, Wang, H, Lin, G et al. (2 more authors) (2020) Unsteady simulation of aircraft electro-thermal deicing process with temperature-based method. Proceedings of the Institution of Mechanical Engineers, Part G: Journal of Aerospace Engineering, 234 (1). pp. 388-400. ISSN 0954-4100

https://doi.org/10.1177/0954410019866066

Unsteady Simulation of Aircraft Electro-thermal Deicing Process with Temperature-based Method

Xiaobin Shen[1,*], Huanfa Wang[1], Guiping Lin[1], Xueqin Bu[1] and Dongsheng Wen[1, 2]

[1] Laboratory of Fundamental Science on Ergonomics and Environmental Control, School of Aeronautic Science and Engineering, Beihang University, Beijing 100191, China

[2] School of Chemical and Processing Engineering, University of Leeds, Leeds LS2 9JT, UK

Abstract

Considering the mass and energy sources carried by the accumulated ice layer, an unsteady heat and mass transfer model of the runback water film on the deicing surface is established to simulate aircraft electro-thermal deicing process. With the extension of the freezing coefficient to the transient calculation, the coupled heat transfer of the runback water and the solid skin is solved at each time step by a temperature-based method. Unsteady numerical simulation is carried out for the electro-thermal deicing system of a NACA 0012 airfoil. The temperature variations with time are in acceptable agreement with the literature data, and the unsteady temperature-based deicing model is verified.

The calculation results of temperature, runback water flux and ice thickness on the deicing surface are analyzed at different time points, and it is shown that the unsteady electro-thermal deicing model can capture the main features of the icing, ice melting and re-freezing processes in the transient deicing simulations.

Keywords

Aircraft icing; Electro-thermal deicing; Unsteady simulation; Freezing coefficient; Runback water

1 Introduction

Aircraft icing, usually caused by the impingement of the super-cooled water droplets on the windward surfaces, seriously threatens flight safety[1]. Ice accretion on the lift surface would damage the aerodynamic shape, resulting in reduced lift and increased drag. Ice layers on other surfaces could also affect aircraft performances, such as maneuverability and stability[2]. Therefore, ice protection systems are always adopted for aircrafts.

Currently, thermal method is the most prominent ice protection strategy used in modern aircrafts[3], and it can be divided into anti-icing approach and deicing way. In anti-icing systems, the heat provided by the engine bleed hot air[4] or the electrical heaters[5] is conducted through the aircraft skin to raise the surface temperature and evaporate the impinging droplets. These systems always keep surface temperature above the freezing point, and prevent the formation of ice on aircraft components. On the other hand, deicing systems allow a small amount of ice accumulated on the protected surfaces. The

adhesion of ice to surface is then destroyed by periodic heating, and ice layers can be removed from aircraft components under the aerodynamic force or centrifugal force[6]. Deicing systems cost much less energy than anti-icing systems[7], and are typically implemented using electrical heating. In addition, the electrical heaters of the thermal deicing systems are usually arranged inside the aircraft component skins, which results in high heating efficiency, short response time and good control performance[8]. The electro-thermal deicing systems are widely used in aircraft tails, helicopter rotors and wind turbine blades.

When an electro-thermal deicing system works, electrical energy is periodically converted into heat to protect aircraft components, while the super-cooled water droplets continually impinge on the component surfaces and freeze into ice. Therefore, the deicing process involves external air-water droplet two-phase flow, runback water film flow on the surface, phase changes between solid ice and liquid water, heat transfer in the ice layer with varying thickness, and unsteady internal heat conduction in the multi-layered skin[9]. It is a complex unsteady multi-phase flow and phase change problem, coupled with heat and mass transfer[10].

At present, most of the studies on the electro-thermal deicing system focused on the heat conduction characteristics of the multi-layered skin and the ice layer, along with the phase transformation process of the ice melting. A series of unsteady solid heat conduction and phase change models have been developed with various solving methods and algorithms[11-15]. However, there are few studies on the unsteady heat and mass transfers of the whole icing, ice melting, deicing and re-freezing processes in flight conditions, and the deicing model still needs to be improved.

Wright[16] developed the governing equation of ice layer in terms of the enthalpy to simulate thermal deicer, and the specific heat capacity was redefined to model the phase change between ice and water. This model has been integrated into LEWICE software. However, since the ice thickness changes from time to time, it is difficult and time consuming to transform ice shape and solve its enthalpy equation for complex surfaces. Subsequently, an electro-thermal deicing experiment was carried out in Lewis Icing Research Tunnel (IRT) of NASA, and the LEWICE/Thermal model was validated[17]. Based on the Myers heat and mass transfer theory[18], the runback water and ice prediction model was extended by Harireche[19] to perform the thermal deicing simulation with ICECREMO2 software, and the surface temperature variation with time was obtained by an explicit finite volume approach. Nevertheless, the Stefan condition was only considered in the ice-water interface of the ice accretion. With FENSAP-ICE software, unsteady deicing simulation was carried out by Reid[20], and the results were in good agreement with the experiment data. However, the heat and mass transfer of the runback water was computed on the uncontaminated geometry, and the effects of the phase change in the ice domain were considered with an appropriate surface projection which was not described in detail. A nose cone electro-thermal anti-icing system was modeled by Ding[21]. The unsteady results matched well with those of the FENSAP-ICE software, but the unsteady deicing model was not explicitly given. Mu[22] established a 3D unsteady model for the thermal deicing simulation, and the results showed agreement with the literature data. However, the effects of the existing ice layer were not tightly coupled in the runback water thermodynamics either. In addition, the surface heat flux from skin heat conduction was extracted to solve the runback water conversation equations and

update the surface temperature. This heat-flux-based method would lead to a non-physical change of the deicing surface temperature from the initial state to the value obtained by the ice accretion calculation under the surface heat flux condition of 0 W in the first time step, no matter how long the time step is.

In general, aircraft electro-thermal deicing is a complex unsteady heat and mass transfer process. There are few studies on its simulation, and the effects of the accumulated ice layer are not tightly coupled with the thermodynamic analysis. In this paper, the water and energy sources of the accumulated ice layer are included in an unsteady heat and mass transfer model of the runback water on the deicing surface, and the coupling solution of the model and the solid skin heat conduction is performed by a temperature-based method. Transient numerical simulations are carried out to verify the unsteady deicing model, and then the heat and mass transfer characteristics in the processes of the icing, ice melting and re-freezing are analyzed in details.

2 Unsteady deicing simulation method

2.1 Simulation procedure for electro-thermal deicing

As the electrical heaters inside the aircraft skin are periodically turned on, the state of the deicing surface changes with time. At each time step, the surface temperature is determined by the coupling of internal skin heat conduction and external air-droplet flow heat transfer. Considering that the ice thickness allowed by the electro-thermal deicing system is relatively thin, the external air flow field and the motion of the super-cooled water droplets are slightly affected by the ice layer on the deicing surface, and they are

assumed unchanged with time[20]. Moreover, the surface temperature varies within a relatively small range, and the air convective heat transfer coefficient is also regarded to be constant during the entire deicing simulation. Therefore, in order to reduce the computational cost and speed up the calculation, the steady-state solution of external air-water droplet flow is used for the unsteady deicing simulation.

The air flow and temperature field around the deicing surface are obtained by solving Reynolds-averaged Navier-Stokes equations (RANS), and the one-equation Spalart-Allmaras (S-A) turbulence model is chosen for good wall-bounded flow results[20]. In order to satisfy the requirements of the S-A turbulence model for solving the boundary layer and the grid independence for convective heat transfer coefficient, the maximum y+ of the air flow mesh should be below one[23]. Assuming that the air and droplet flows are one-way coupled, the influence of air flow on the motion and impingement characteristics of water droplets is modeled, and Eulerian method[24] is applied to obtain the local water droplet collection efficiency. The calculations of the air and water droplet flow fields are all carried out by the SIMPLE algorithm with second-order upwind scheme in the CFD solver FLUENT[23].

The heating energy generated by the heaters is conducted through the internal solid skin, and heats the deicing surface periodically. The different material properties of the multi-layered skin structure are considered, and unsteady heat transfer in each layer is solved by the solid heat conduction differential equation:

$$\rho \mathrm{c_p} \frac{\partial \mathrm{T}}{\partial \mathrm{t}} = \nabla \cdot \left(\lambda \nabla \mathrm{T} \right) + \mathrm{S} \qquad (1)$$

where ρ is the density of the material, c_p is the specific heat, t is the time, T is the temperature, λ is the thermal conductivity, and S is the heat source term.

The external air-water droplet flow interacts with the internal solid skin heat conduction by the water film on the deicing surface, thus the heat and mass transfer model of the runback water is always used to couple the internal and external heat exchange[25]. Since the convective heat transfer coefficient and the local water droplet collection efficiency are obtained by the steady-state external solution, the unsteady heat transfer calculation for the deicing process is simplified to the coupling of the runback water thermodynamics and the skin heat conduction.

In this paper, the effects of the accumulated ice layer are included in the conservation equations of the runback water, which will be described in detail in section 2.2. Moreover, the coupling is performed by a temperature-based method. For the iterative calculation at a time step, the deicing surface temperature calculated by the solid skin heat conduction equation is extracted to solve the thermodynamic model of the runback water, and the corresponding deicing heat load can be obtained. Then, the heat load is added to the heat conduction differential equation of the solid skin as a Neumann boundary condition, and the equation is applied to update the temperatures of the deicing surface and entire skin. Convergence in the current time step is achieved when surface temperature deviation between the iterations meets the setting value. The skin temperature and ice thickness at the current time are saved, and then the iteration for the next time step is carried out until the entire deicing simulation is completed. The specific procedures for the unsteady electro-thermal deicing calculation are presented in Figure 1.

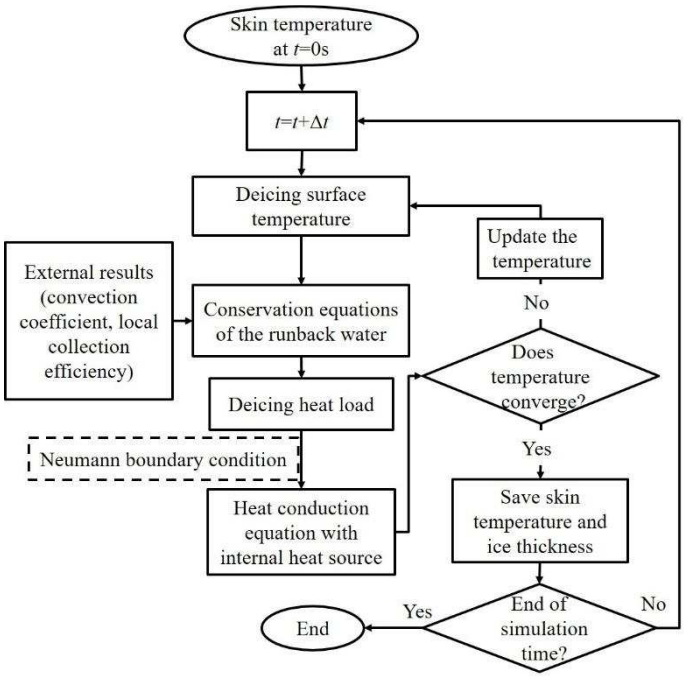

Figure 1. Flow chart for unsteady deicing simulation with temperature-based method.

2.2 Unsteady heat and mass transfer model

Heat and mass transfer analysis is performed for the whole solid and liquid water in a control volume (CV) on the electro-thermal deicing surface, as shown in Figure 2. In addition to the diffusion term of the energy equation and the convection terms caused by water flow, the changes of the water quality and energy in the CV are also affected by various mass and heat sources. The mass sources of the whole water in the CV include the impinging water flow rate $\dot{m}_{imp}$ and the water evaporating rate $\dot{m}_{evap}$. Meanwhile, the energy sources consist of: heat flow rate of impinging water $\dot{Q}_{imp}$, evaporative heat flow rate $\dot{Q}_{evap}$, convective heat flow rate $\dot{Q}_{c}$, and deicing heat flow rate $\dot{Q}_{deice}$ needed for the given surface temperature. Therefore, the unsteady control equations of the whole water in the CV on the electro-thermal deicing surface could be obtained by the mass and energy conservations:

$$\begin{cases} \dfrac{\partial m_w}{\partial t} + \nabla\left(m_w \mathbf{V}_w\right) = \dot{m}_{imp} - \dot{m}_{evap} \\ \dfrac{\partial E_w}{\partial t} + \nabla\left(E_w \mathbf{V}_w\right) = \nabla\cdot\left(\lambda_w \nabla T_s\right) + \dot{Q}_{deice} + \dot{Q}_{imp} - \dot{Q}_c - \dot{Q}_{evap} \end{cases} \tag{2}$$

where m_w is the total amount of the whole solid and liquid water deposited in the CV, E_w is the total energy carried by the water in the CV, $\mathbf{V}_w$ is the water velocity vector, λ_w is the thermal conductivity of the whole solid and liquid water, and T_s is the temperature of the CV.

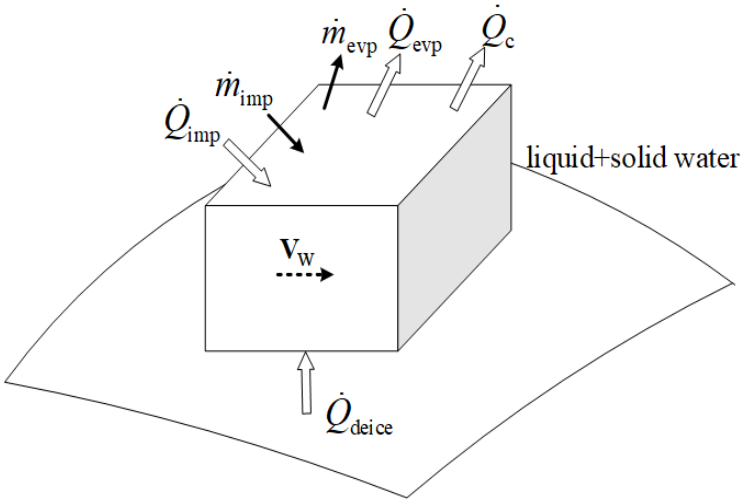

Figure 2. Heat and mass transfer of the whole water in a CV on the deicing surface.

Since the water in the CV includes both liquid water and solid ice, its heat and mass transfer processes are very complicated because of the different heat exchange and flow characteristics of the solid and liquid states. The parameters in the conservation equations are difficult to determine, and the equations cannot be solved directly. Based on the Messinger model[26], the following assumptions are made according to the settings of LEWICE [16] and FENSAP [20]: (1) All the liquid water in the CV would run back outwards, while the solid ice does not move and would accumulate on the deicing surface; (2) The enthalpy of the liquid water at the freezing point of 273.15 K is assumed to be zero; (3)

The temperatures of the deicing surface, the ice layer and the runback water are the same with the value of the CV T_s, and the lateral heat conduction between the CVs along the deicing surface is ignored; (4) The heating energy would first melt the accumulated ice layer, and then prevent the impinging water droplets from freezing; (5) The liquid water formed by the ice melting is removed from the CV, and would not participate in the runback water flow; (6) Ice breakage and shedding during the deicing process are not considered.

It can be found from the assumption (1) that the total amount of the whole water stayed in the CV m_w equals to that of the accumulated ice layer m_{ice}, and the enthalpy of the ice layer E_{ice} is the total energy of the whole water on the CV E_w. In addition, since the ice layer does not move, the convection terms of the conservation equations are determined by the liquid runback water. In two-dimensional calculation, the water film flows along the airfoil, and there are:

$$\begin{cases} \nabla\left(\mathrm{m_w}\mathbf{V}_\mathrm{w}\right) = \dot{\mathrm{m}}_{\mathrm{out}} - \dot{\mathrm{m}}_{\mathrm{in}} \\ \nabla\left(\mathrm{E_w}\mathbf{V}_\mathrm{w}\right) = \dot{\mathrm{Q}}_{\mathrm{out}} - \dot{\mathrm{Q}}_{\mathrm{in}} \end{cases} \tag{3}$$

where $\dot{\mathrm{Q}}_{\mathrm{in}}$ and $\dot{\mathrm{Q}}_{\mathrm{out}}$, respectively, are the heat flow rates carried by the mass flow rates of the runback water entering the current CV $\dot{\mathrm{m}}_{\mathrm{in}}$ and flowing out the CV $\dot{\mathrm{m}}_{\mathrm{out}}$. According to the assumption (2), there are:

$$\dot{\mathrm{Q}}_{\mathrm{in}} = \dot{\mathrm{m}}_{\mathrm{in}} \cdot \mathrm{c}_{\mathrm{p,w}} \cdot (\mathrm{T}_{\mathrm{in}} - \mathrm{T}_{\mathrm{ref}}) \tag{4}$$

$$\dot{\mathrm{Q}}_{\mathrm{out}} = \dot{\mathrm{m}}_{\mathrm{out}} \cdot \mathrm{c}_{\mathrm{p,w}} \cdot (\mathrm{T}_{\mathrm{s}} - \mathrm{T}_{\mathrm{ref}}) \tag{5}$$

where $c_{p,w}$ is the specific heat of liquid water, T_{in} is the temperature of the upstream CV, and T_{ref} is the freezing point temperature of 273.15 K.

Moreover, it is known from the assumption (3) that the diffusion term of the energy

equation is zero. Based on those derivations mentioned above, the implicit difference scheme is used to discretize the mass and energy conservation equations of runback water, and Eq. (2) becomes:

$$\begin{cases} \dfrac{m_{ice}^{i} - m_{ice}^{i-1}}{\Delta t} = \dot{m}_{imp} + \dot{m}_{in} - \dot{m}_{evap} - \dot{m}_{out} \\ \dfrac{E_{ice}^{i} - E_{ice}^{i-1}}{\Delta t} = \dot{Q}_{deice} + \dot{Q}_{imp} + \dot{Q}_{in} - \dot{Q}_{c} - \dot{Q}_{evap} - \dot{Q}_{out} \end{cases} \tag{6}$$

where Δt is the time step, and the superscript i indicates the parameter of the i-th time step. The parameters without superscript are the ones of the i-th time step. It can be seen that the mass and energy sources carried by the accumulated ice layer are tightly coupled in the runback water thermodynamic model.

Based on the Eulerian method[24], the impinging water flow rate can be obtained by:

$$\dot{m}_{imp} = \beta \cdot U_{\infty} \cdot LWC \cdot \Delta s \tag{7}$$

where β is the local water droplet collection efficiency, U_∞ is the flight velocity, LWC is the liquid water content, and Δs is the surface area of the CV.

Meanwhile, $\dot{Q}_{imp}$ consists of the enthalpy and the kinetic energy of the impinging droplets, as expressed as:

$$\dot{Q}_{imp} = \dot{m}_{imp} \cdot \left[\frac{U_{\infty}^{2}}{2} + c_{p,w} \cdot (T_{\infty} - T_{ref}) \right] \tag{8}$$

where T_∞ is the ambient static temperature.

The water evaporating rate could be determined by the Chilton-Colburn analogy theory[27]:

$$\dot{m}_{evap} = \Delta s \cdot \frac{h_s}{c_{p,air}} \cdot \left(\frac{Pr}{Sc} \right)^{2/3} \cdot \frac{M_v}{M_{air}} \cdot \left[\frac{p_{v,sat}(T_s) - p_{v,e}}{p_e - p_{v,e}} \right] \tag{9}$$

where h_s is the air convective heat transfer coefficient, $c_{p,air}$ is the specific heat of air, Pr is the Prandtl number, Sc is the Schmidt number, M_v and M_{air} are the molecular weight of water and air, respectively. $p_{v,sat}(T_s)$ is the saturated evaporative pressure at the local surface temperature, $p_{v,e}$ is the vapor pressure at the edge of boundary layer, and p_e is the static pressure at the edge of boundary layer.

Then, $\dot{Q}_{evap}$ could be obtained by:

$$\begin{cases} \dot{Q}_{evap} = \dot{m}_{evap} \cdot \left[i_{sv} + c_{p,ice} \cdot (T_s - T_{ref}) - i_{ls} \right] & T_s < T_{ref} \\ \dot{Q}_{evap} = \dot{m}_{evap} \cdot \left[i_{lv} + c_{p,w} \cdot (T_s - T_{ref}) \right] & T_s \geq T_{ref} \end{cases} \tag{10}$$

where i_{sv} is the latent heat of sublimation, $c_{p,ice}$ is the specific heat of ice, i_{ls} is the solidification latent heat, and i_{lv} is the latent heat of vaporization.

Convective heat flow rate can be obtained by the convective heat transfer coefficient and the temperature difference:

$$\dot{Q}_c = h_s \cdot (T_s - T_{ad}) \cdot \Delta s \tag{11}$$

where T_{ad} is the reference surface temperature calculated with adiabatic condition for the skin.

The enthalpy of the ice layer accumulated in the CV is also computed referring to the water at the freezing point, as expressed as:

$$E_{ice}^{i} = m_{ice}^{i} \cdot \left[c_{p,ice} \cdot (T_s^{i} - T_{ref}) - i_{ls} \right] \tag{12}$$

In an unsteady simulation, the initial condition is given, and then the parameters at the time step of i-1 is known when solving the equations of the i-th time step. For the iterative process at each time step, the deicing surface temperature calculated by the solid heat conduction is extracted as a known parameter in the temperature-based method, and the heat and mass conservation equations of the runback water are solved for the

corresponding deicing heat load $\dot{Q}_{deice}/\Delta s$. According to the relationship between the solid-liquid state of the water film and the freezing point, the deicing surface temperature T_s^i can be divided into three cases to solve the conservation equations: at the freezing point, above the freezing point and below the freezing point.

Water solidification is assumed to happen over the small temperature range from T_{ref} to $T_{ref}+\Delta T$, and ΔT is an artificial temperature range between water and ice phases[28]. Therefore, when the deicing surface temperature T_s^i is within the range of 273.15K to 273.15K+ΔT, it is considered to be at the freezing point, and the liquid water and the solid ice are simultaneously present in the CV. Considering the influence of the existing ice layer, the definition of the freezing coefficient f is extended to the unsteady deicing calculation, and f indicates the ratio of the ice quality to the whole water in the CV at the time step of i:

$$f = \frac{m_{ice}^i/\Delta t}{\dot{m}_{in} + \dot{m}_{imp} + m_{ice}^{i-1}/\Delta t - \dot{m}_{evap}} \quad (13)$$

Based on Domingos[28] and Wright[29], the freezing fraction f is related to the artificial temperature range ΔT, as expressed below.

$$f = 1 - \frac{T_s - T_{ref}}{\Delta T} \quad (14)$$

From Eq. (13) and Eq. (14), it can be obtained that:

$$\frac{m_{ice}^i}{\Delta t} \cdot \Delta T = \left(\dot{m}_{in} + \dot{m}_{imp} + \frac{m_{ice}^{i-1}}{\Delta t} - \dot{m}_{evap} \right) \left(T_{ref} - T_s + \Delta T \right) \quad (15)$$

By solving Eq. (6) and Eq. (15), the deicing heat load $\dot{Q}_{deice}/\Delta s$ at freezing point can be obtained. It is known from the assumption (4) that the heating energy is used to melt the existing ice rather than preventing water freezing. Therefore, the accumulated ice

layer at the time step of i-1 might melt as a result of the electrical heating power, but at the same time, the ice layer could grow outwards due to the impact of super-cooled water droplets. After all the existing ice melts, the excess heat then reduces the droplet freezing rate at the time step of i, since ice shedding is not considered according to the assumption (6). In addition, based on the setting of FENSAP-ICE and the assumption (5), the liquid water formed by ice melting is removed from the runback water flow rate $\dot{m}_{out}$ flowing out of the CV.

When $T_s^i > 273.15\text{K}+\Delta T$, the deicing surface temperature is higher than the freezing point, thus there is no ice in the CV and the conservation equations become:

$$\begin{cases} \dfrac{m_{ice}^{i-1}}{\Delta t} + \dot{m}_{imp} + \dot{m}_{in} - \dot{m}_{evap} - \dot{m}_{out} = 0 \\ \dfrac{E_{ice}^{i-1}}{\Delta t} + \dot{Q}_{deice} + \dot{Q}_{imp} + \dot{Q}_{in} - \dot{Q}_c - \dot{Q}_{evap} - \dot{Q}_{out} = 0 \end{cases} \tag{16}$$

In this condition, all the ice layer is melted. According the assumption (5), the outflow runback water flow rate $\dot{m}_{out}$ is reduced by the melting ice $m_{ice}^{i-1}/\Delta t$.

When $T_s^i < 273.15\text{K}$, the runback water in the CV is completely frozen with no water flowing out, and the conservation equations become:

$$\begin{cases} \dfrac{m_{ice}^{i}}{\Delta t} = \dfrac{m_{ice}^{i-1}}{\Delta t} + \dot{m}_{imp} + \dot{m}_{in} - \dot{m}_{evap} \\ \dfrac{E_{ice}^{i}}{\Delta t} = \dfrac{E_{ice}^{i-1}}{\Delta t} + \dot{Q}_{deice} + \dot{Q}_{imp} + \dot{Q}_{in} - \dot{Q}_c - \dot{Q}_{evap} \end{cases} \tag{17}$$

To sum up, the deicing heat load $\dot{Q}_{deice}/\Delta s$ and the accumulated ice layer m_{ice}^{i} can be obtained based on the different deicing surface temperature conditions by solving corresponding heat and mass conservation equations of the runback water. Then, the ice thickness at current time H^i can be calculated by:

$$H^i = \frac{m_{ice}^i}{\rho_{ice} \cdot \Delta s} \quad (18)$$

where ρ_{ice} is the density of ice.

3 Numerical simulation

3.1 Geometry and Conditions

In order to verify the unsteady model, a NACA 0012 airfoil electro-thermal deicing system is selected for numerical simulation from rare open literature[17]. The experiments of this system were conducted in the Lewis IRT, and the experimental results have been used to validate the unsteady deicing models of LEWICE/Thermal and FENSAP-ICE software. The NACA 0012 airfoil has a chord length of 0.9144 m, and the specific geometric model is shown in Figure 3. There are seven heaters with different lengths arranged around the leading edge inside the skin, and the heating power of each can be controlled individually. Due to manufacturing difficulties, the seven heaters are not symmetrically installed, but are offset by about 4.572 mm from the leading edge. The specific positions of the heaters are as listed in Table 1, where the dimensionless distance s/c = 0 means the leading edge of the airfoil, and s/c is positive for the upper airfoil surface.

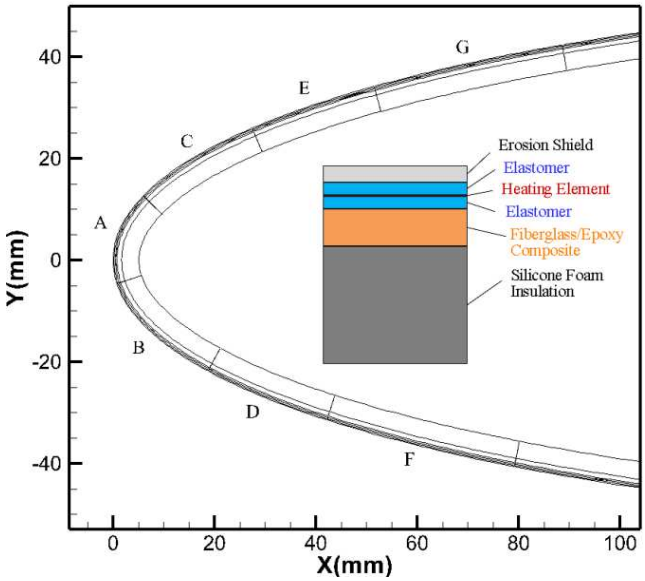

Figure 3. Geometry and heaters of the electro-thermal deicing system.

Table 1. Positions of the heating elements[17].

Heater	F	D	B	A	C	E	G
Start_s/c	-0.1024	-0.0607	-0.0329	-0.0051	0.0157	0.0435	0.0713
End_s/c	-0.0607	-0.0329	-0.0051	0.0157	0.0435	0.0713	0.1129

As shown in Figure 3, the multi-layered skin structure of the electro-thermal deicing system is made of 6 layers, and Table 2 lists their material properties and thicknesses. The energy generated by the electrical heating layer is transferred to the outer skin surfaces by means of heat conduction. Since the total thickness and thermal resistance of the layers outside the heating elements are small while the values of the inner layers are large, the heating energy is mainly transferred outwards and the heat leakage to the inner surface of the skin is very small.

Table 2. Material properties of the skin[17].

Material	λ (W/m/K)	ρ (kg/m^3)	c_p (J/kg/K)	Thickness (mm)
Heating Element(alloy 90)	41.018	8906.26	385.112	0.0127
Erosion Shield(SS 301 HH)	16.269	8025.25	502.32	0.2032
Elastomer(COX 4300)	0.256	1383.99	1255.8	0.2794
Fiberglass/Epoxy Composite	0.294	1794.07	1569.75	0.889
Silicone Foam Insulation	0.121	648.75	1130.22	3.429

Case 1 and Case 2 in Ref. 17 are chosen for unsteady deicing simulation. The boundary conditions of the external air flow and super-cooled water droplets motion are the same for both cases: the flight velocity is 44.7 m/s with angle of attack (AOA) of 0 °, the ambient temperature is -7.6 °C, *LWC* is 0.78 g/m^3, and the water droplet diameter is 20 μm. The initial temperature of the solid skin is set to be the ambient temperature of -7.6 °C, and there is no ice layer accumulated on the deicing surface at the beginning of the simulation.

The heater cycle of 120 s is performed for the electro-thermal de-icing system. Heater A is a heat blade with an electrical power of 7.75 kW/m^2, and it is activated during the whole deicing process. The other heaters are used to deicing, and work for only 10 s throughout each cycle. For Case 1, the heaters B and C have a heating power of 15.5 kW/m^2 and are activated from 100 s to 110 s, while the heating powers of the heaters D-G are 12.4 kW/m^2 and the heaters work from 110 s to 120 s at every cycle. For Case 2, the turn on time points of the heaters B-G are the same with those of Case 1, but the

heating powers are all set to be 10.85 kW/m^2.

3.2 Verification of the deicing model

Figure 4 shows the local water droplet collection efficiency and convective heat transfer coefficient of the NACA0012 airfoil for electro-thermal deicing simulation, and the results are not updated during the entire unsteady calculation. It can be seen that since the AOA is 0 °, the curves are symmetric along the upper and lower surfaces. The results both reach their maximum values at the leading edge of the airfoil. As the distance from the leading edge increases, the local collection efficiency β declines to 0 with the water droplet impingement limits at the positions of s/c=±0.033, while the convective heat transfer coefficient decreases to a low value and then increases due to the boundary layer transition. The external air-droplet flow results obtained by RANS and Eulerian method were already used for anti-icing calculations, and the solutions agreed well with the experimental data[30]. Therefore, they are considered to be accurate for the unsteady deicing calculation.

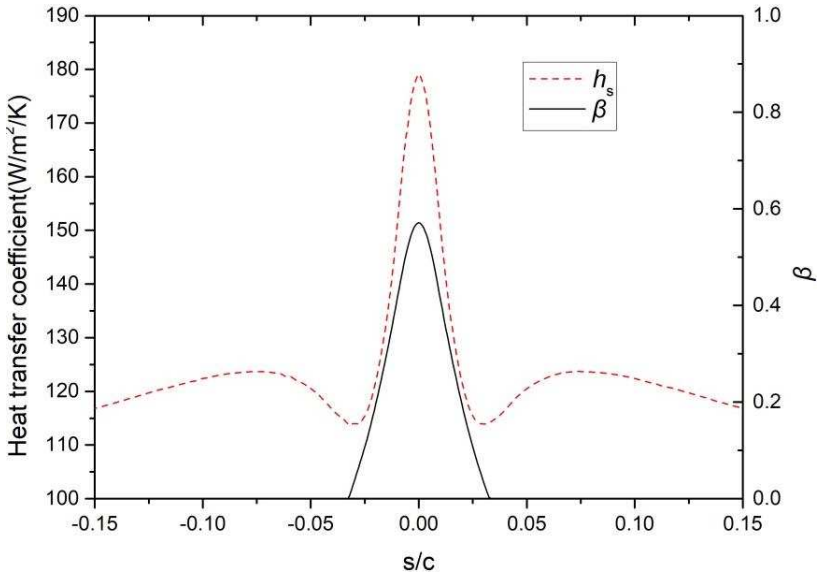

Figure 4. Local collection efficiency and heat transfer coefficient[30].

At each time step, the external and internal coupling heat transfer model is solved with relaxation coefficient to guarantee the convergence, and the calculation converges slowly, especially when the CV is in the mush zone of the freezing point. Figure 5 presents the temperature changes of the heaters for Case 1 and Case 2 with the time steps of 1 s, 0.5 s and 0.25 s. Since the heating time of the deicing cycles are the same for Case 1 and Case 2, their temperature trends are similar. When a heater is turned on, the corresponding temperature would rise quickly. It can be found that the temperature curves for each heater are all in good agreement, indicating that the established unsteady deicing model is slightly affected by the time step. In order to reduce the calculation time, the time step of 1 s is used for the simulation and analysis of the entire electro-thermal deicing processes.

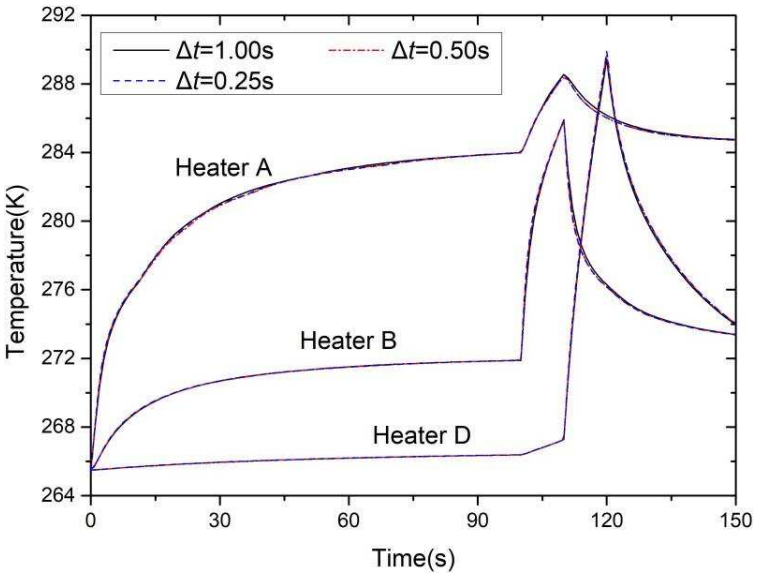

(a) Case 1

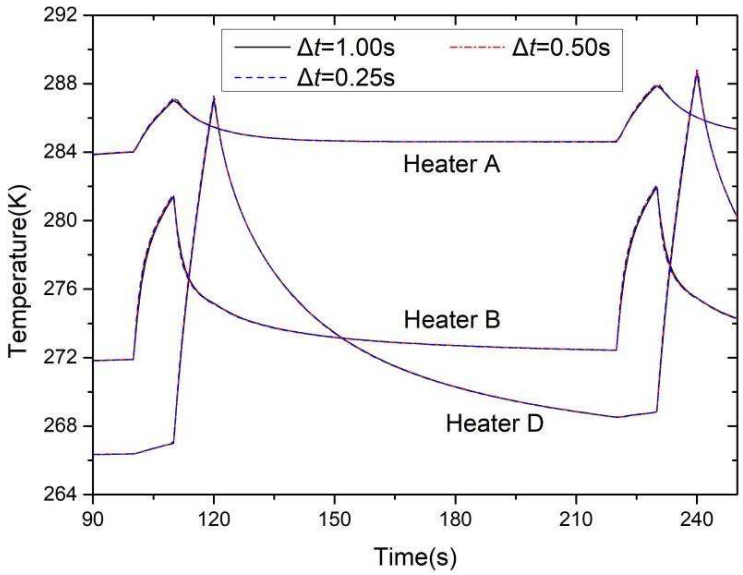

(b) Case 2

Figure 5. Temperature results with the time steps of 1, 0.5, and 0.25 s.

Figure 6 presents the comparisons of the temperature variations with the literature data of the heater B for Case 1 and Case 2. Since the heaters are arranged asymmetrically along the upper and lower airfoil, the temperature curves of the heaters B and C are listed in the same figure, and they performed differently. For Case 1, the highest and the lowest predicted temperatures of the heater C are closer to the experiment results of the heater B, while the predicted maximum temperature of the heater B is smaller but the temperature drop curve agrees better with those of LEWICE[17] and FENSAP-ICE[20]. It can also be seen from Figure 6a that the initial state vanishes after the first deicing cycle, and then the heater temperatures change periodically. For Case 2, there is only the data of the first cycle available for comparison. As shown clearly in Figure 6b, the predicted temperature rise rate and the peak of the heater C also match better with the experiment measurements of the heater B, while the predicted drop rate of the heater B is closer to the curve of LEWICE. It should be noted from the comparison of the asymmetric offset direction in

Ref. 20 that the results obtained by FENSAP-ICE were also the temperature changes of the heater C, which were consistent with the experiment data of the heater B.

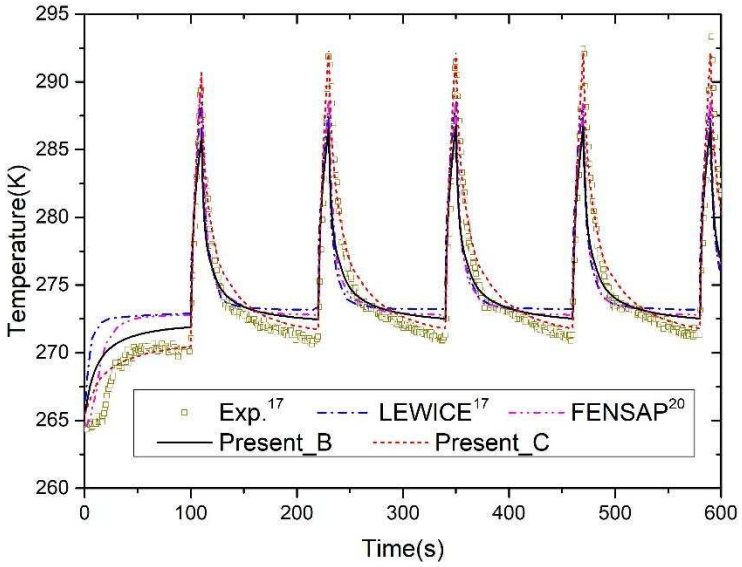

(a) Case 1

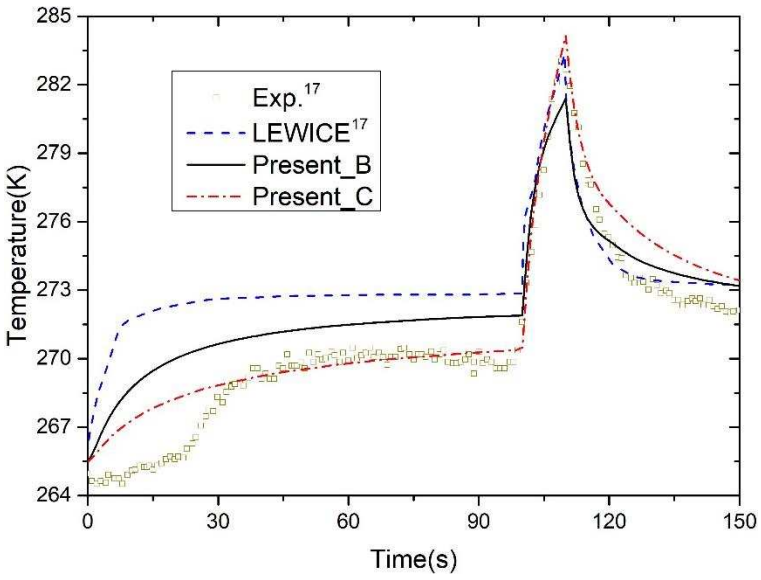

(b) Case 2

Figure 6. Comparison of temperature change with literature data of the heater B.

Since electro-thermal deicing process is a complex unsteady heat transfer problem, the temperature error may occur according to the following reasons: 1) It is difficult to

get the exact external air-droplet flow results, and then the errors would accumulate in the process of unsteady calculation. In addition, the runback water flow along the deicing surface would further enlarge the temperature deviations for the downstream locations; 2) The established model does not take into account the ice shedding, and the presence of ice layer would make the predicted temperature lower at the icing area but higher at downstream location; 3) The temperature distributions in the water film and the icing layer are not considered, which affects conjugate heat transfer characteristics. Generally, the temperature result obtained by the unsteady electro-thermal deicing model matches acceptably with the literature data, and the present model and the temperature-based method are verified.

4 Analysis and Discussion

4.1 Icing process

Ice accretion may occur at different places during the whole deicing simulation. The icing process analyzed here is the time before 100 s in the first deicing cycle, and it starts with low initial skin temperature. Since the conditions of the external air-droplet flow and the heating power of the heater A are the same for Case 1 and Case 2, their icing processes are identical. Figure 7 presents the temperatures, runback water fluxes and ice thicknesses on the deicing surface at different icing moments. As the initial skin temperature is much lower than the freezing point, the surface temperature is still below 273.15 K after the heater A is turned on for 1 second, and the impinging water droplets all freeze into a thin ice layer instantly without any runback water. In the temperature-based

method, the latent energy released by icing is added to the skin heat conduction as a Neumann boundary, and the surface temperature within the impingement range would rise under the combined influences of the electrical heating and the latent heat. Therefore, the non-physical temperature change of the heat-flux-based method[22] is avoided in the calculation of the first time step.

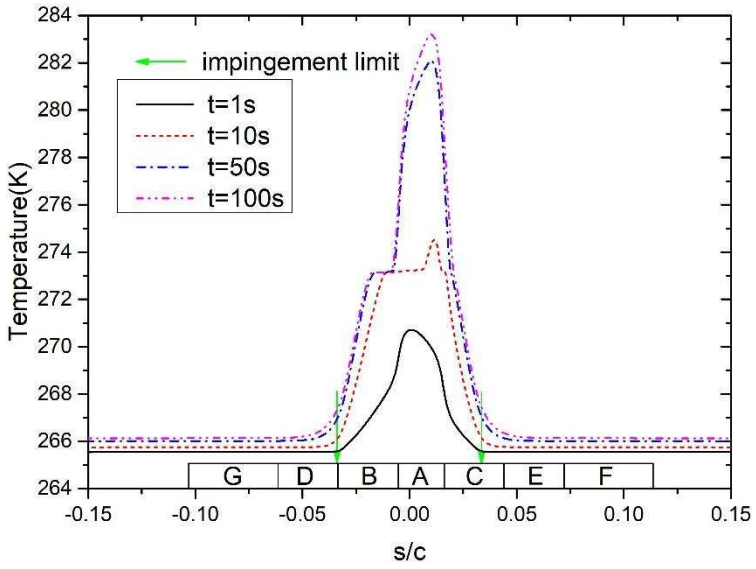

(a) Surface temperature distributions.

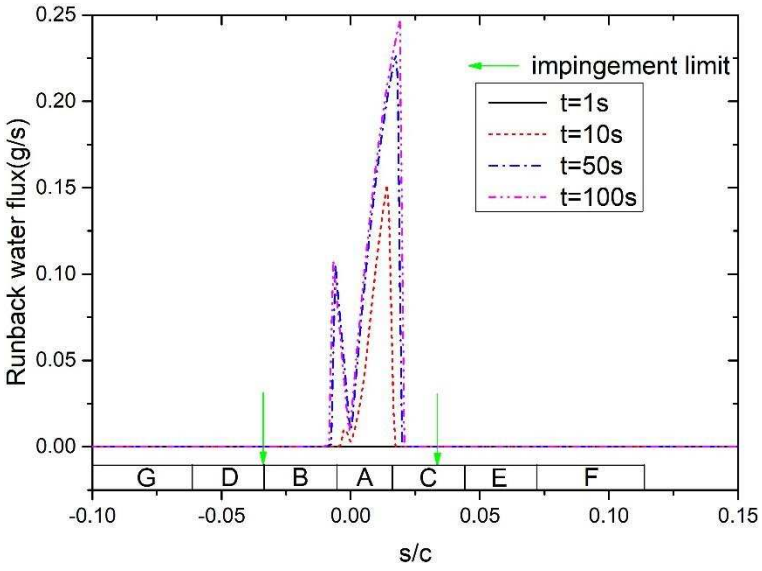

(b) Runback water flux distributions.

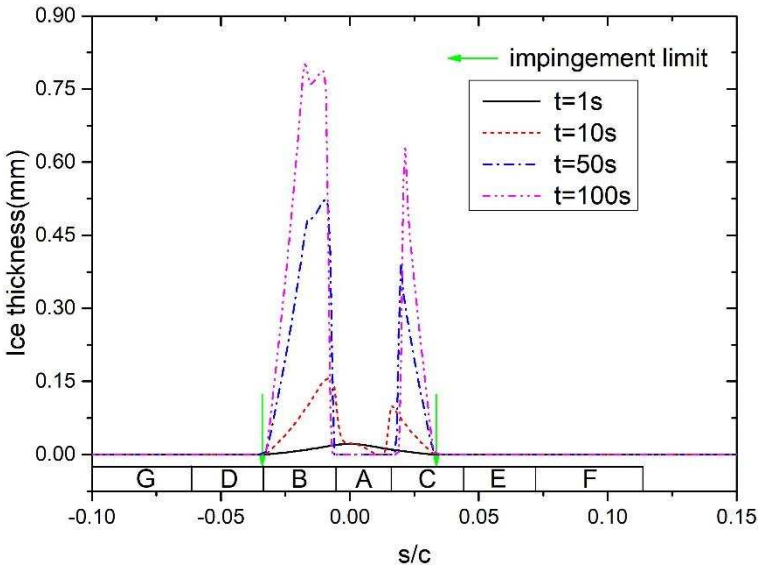

(c) Ice thickness distributions.

Figure 7. Results at different times in the icing process.

As time increases, the energy generated by the heat blade of the heater A gradually reaches the outer skin surface, and the rising temperature would melt the existing ice layer, and prevent the impinging water droplets from freezing in the heated area. At 10 s, the surface temperature is around the freezing point with some part above 273.15 K, and the thin ice layer over the heater A begins to melt with runback water formed on the deicing surface. Since droplet impingement range is larger than the heated area of the heater A, the runback water over the heater A would flow backwards, and freeze into ice layer together with the collected water droplets on the outside surfaces of the heaters B and C.

At the time of 50 s, the surface temperature over the heater A is all above the freezing point, and no ice is observed there. The amount and range of the runback water become larger, while the ice layers over the heaters B and C keep growing. In addition, since the initial skin temperature is set to the ambient static temperature, the temperature

of the boundary layer around the airfoil would be higher than the initial value as a result of the aerodynamic heating. Therefore, as shown in Figure 7a, the surface temperature without the influences of the impinging water and the electrical heating would also gradually increase with time due to the air convective heat transfer, which was also described in Ref. 20.

The differences of the surface temperature and runback water flux between 50 s and 100 s are slight, and the increase of the ice thickness is stable, meaning that the thermal equilibrium of the icing process approaches steady state. Figure 8 shows the temperature distribution in the solid skin at 100 s. Due to the asymmetric layout of the heaters, the temperature on the upper surface is higher than that on the lower one, but the temperature rise regions on both surfaces are similar due to the same size of the droplet impingement ranges. In addition, it could be seen from Figure 7 that in the icing process, the runback water flux and its range are larger on the upper surface, while the icing area and ice thickness are smaller there. There is no runback water outside the droplet impingement range, and the ice layers are all within the impingement limits.

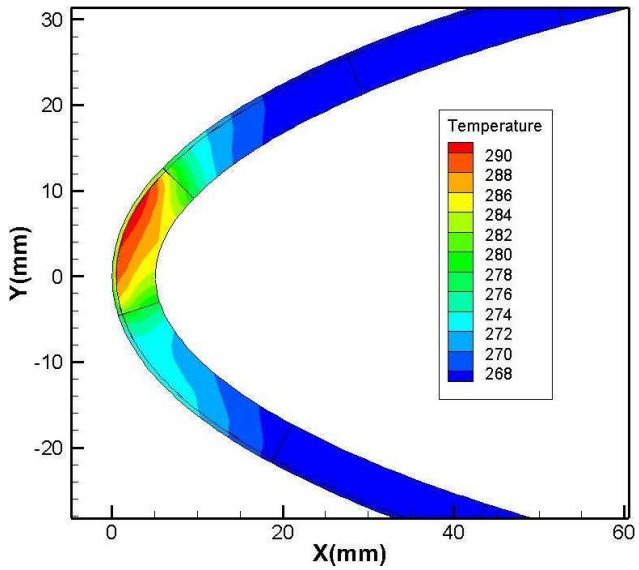

Figure 8. Contour of temperature (K) in the solid skin at 100 s.

4.2 Ice melting process

After the heaters B and C are turned on at 100 s, the heating energy increases their outside surface temperatures, and the ice melting process begins for the deicing system, as shown in Figure 9. Since the electrical deicing powers of Case 1 are greater than those of Case 2, its surface temperatures over the heaters B and C are higher at the time of 110 s. Since ice breakage and shedding are not considered, the accumulated ice layer has great influence on the temperature distribution. It can be seen from Figure 9 that at 110 s, the ice thicknesses are reduced a lot from those of 100 s for Case 1, while the decreases of the ice layers and their ranges for Case 2 are relatively small. Therefore, the runback water range of Case 1 becomes larger on the upper surface, while that of Case 2 changes slightly from that at 100 s. As the ice layers on the surfaces are not melted completely for both cases, the lowest surface temperature over the heaters B and C is kept at the freezing point.

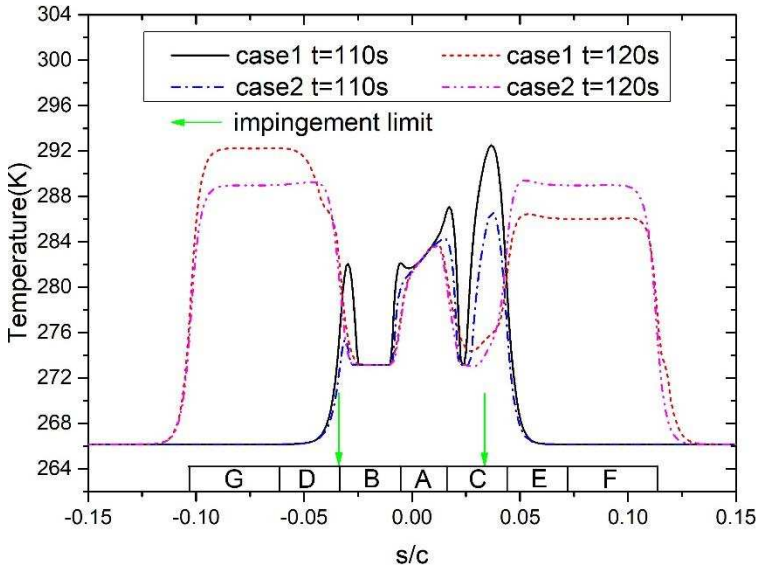

(a) Surface temperature distributions.

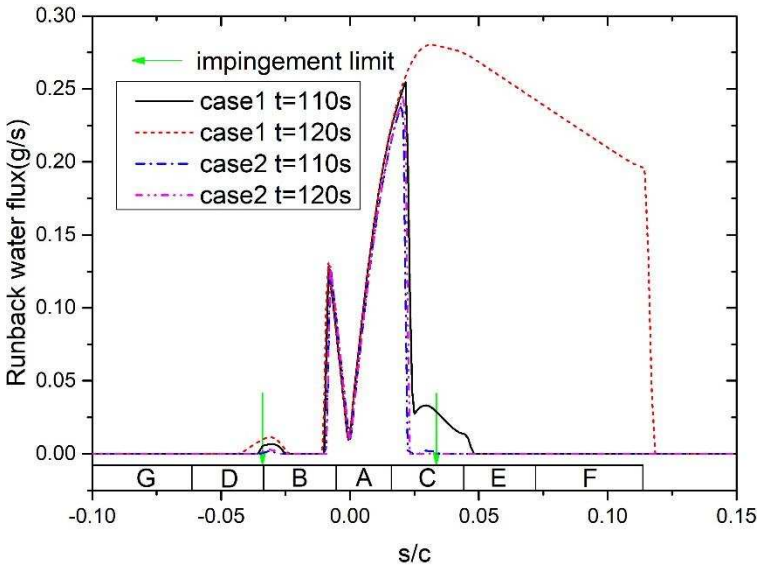

(b) Runback water flux distributions.

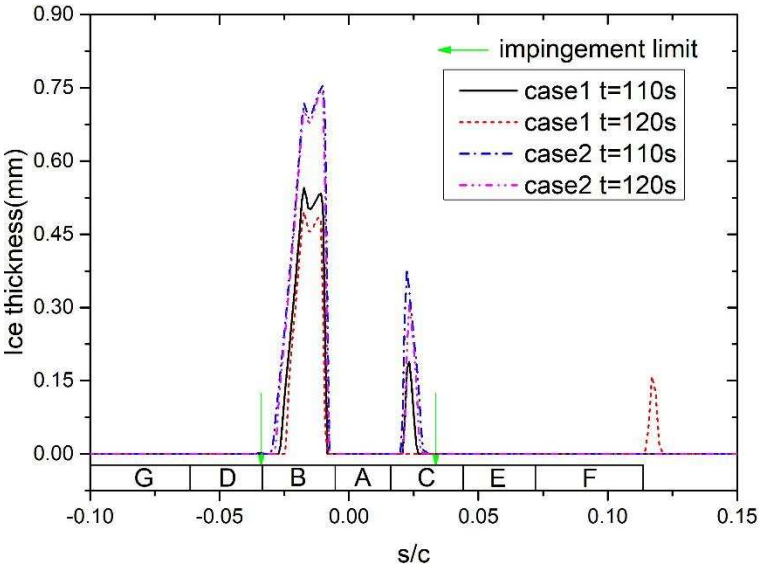

(c) Ice thickness distributions.

Figure 9. Results at different times in the ice melting process.

The runback water flux and its range on the lower surface are small for both cases at 110 s, and the surface temperature is also lower there, as shown in Figure 9. There are two reasons for that. Firstly, the icing area and ice thickness on the lower surface were larger before the two deicing heaters are turned on, so more heating energy is used to

melt the accumulated ice layer. Secondly, since the heater B is closer to the leading edge than the heater C due to the asymmetric arrangement, convective heat transfer coefficient over the heater B is larger, and the resulting greater evaporative and convective heat flow rates make more impinging water droplets freeze at the lower surface.

Since the skin temperatures around the heater B and C are quite high at 110 s, the ice layers keep melting after the heaters are turned off. The ice thicknesses over the heaters B and C are smaller at 120 s for both cases, and there is even no ice for Case 1 over the heater C where the lowest surface temperature increases above 273.15 K. The downstream temperatures go up with the heaters D-G activated. For Case 2, the surface temperatures over the heaters D-G are all high at 120 s, because there is almost no runback water flow into those ranges from upstream surfaces. For Case 1, the runback water on the outside surface of the heater C flows through the downstream surfaces over the heaters E and F, and freezes into an ice ridge away from the protected area, which was also found on the upper airfoil surface in Ref. 20. Under the influence of the runback water, the upper surface temperature of Case 1 is lower than that of Case 2, even though the heating powers are larger. However, the runback water range of Case 1 is also small on the lower surface at 120 s, and the temperature there is very high with no ice ridge formed outside the lower heated area.

Figure 10 presents the contours of the skin temperature at 120 s for both cases. It can be seen clearly that the upper skin of Case 1 has higher temperature than the lower one, while the temperatures of the heaters D-G for Case 2 are at the similar level with dry outer surfaces. At this time, the temperatures around the heaters B and C are low for both cases. In addition, the inner skin temperatures under the deicing heaters are low with

small temperature gradient, while the outer skins have high temperature gradients, indicating most of the deicing energy is transferred outwards. The unsteady temperature distributions in the skin are affected by the material properties of the multi-layered structure and the control law of the electro-thermal deicing heaters.

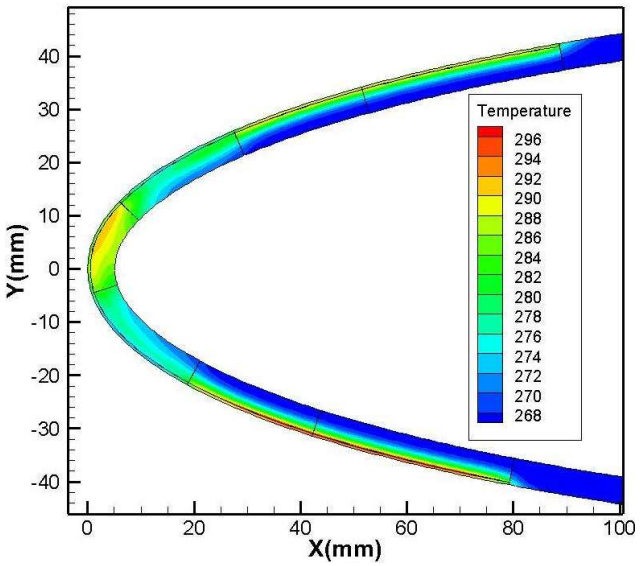

(a) Case 1

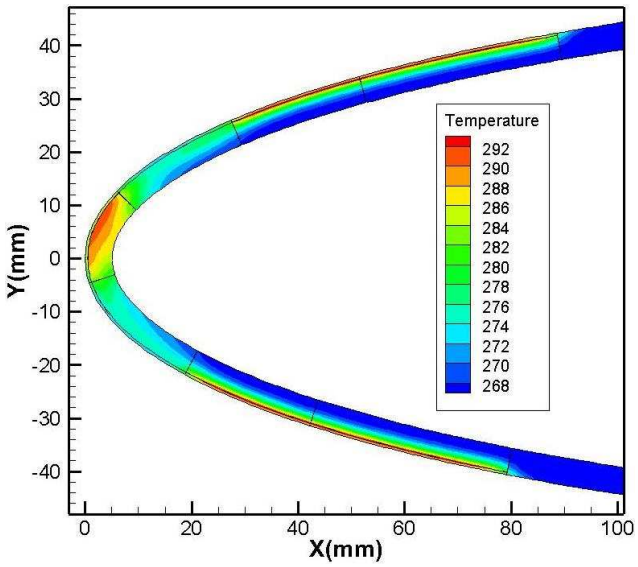

(a) Case 2

Figure 10. Contour of temperature (K) in the solid skin at 120 s.

4.3 Re-freezing process

Unlike icing process, re-freezing one begins with very high skin temperature when the heaters B-G are turned off. With the decreasing surface temperature, this process starts at 110 s for the surfaces over the heaters B and C, while the beginning time for those of the heaters D-G is 120 s. Since the runback water does not flow out of the heated areas over the heaters B and C for Case 2, the surfaces over heaters D-G are dry, and the distribution of the runback water flux changes slightly after 120 s. The surface temperatures just drop with time, and the ice layers become thicker at the fixed positions over the heaters B and C, as shown in Figure 11. The situation is the same for the lower surface of Case 1, but the ice thickness is smaller because more ice layer has been melted under the larger heating power of Case 1. For the upper surface of Case 1, runback water film flows over the heaters E and F at 120 s. When the surface temperature decrease to the freezing point, the runback water becomes solid ice, and could not flow backwards any more. As can be seen from Figure 11b and Figure 11c, the runback water range on the upper surface shrinks with time, and the ice layer appears again over the heater C at 140 s. Moreover, the re-freezing ice area is larger than that of the icing process due to the larger runback water range.

At the time of 160 s, the surface temperature is all below the freezing point except the protected area over the heater A. At this time, the runback water range is reduced to the value of 100 s, and the ice layer become thicker only in the water droplet impingement range, indicating that the ice accretion of the re-freezing process approaches steady. After that, the skin temperature would further decrease and the ice layer would be thickened until the heaters B-G are turned on again.

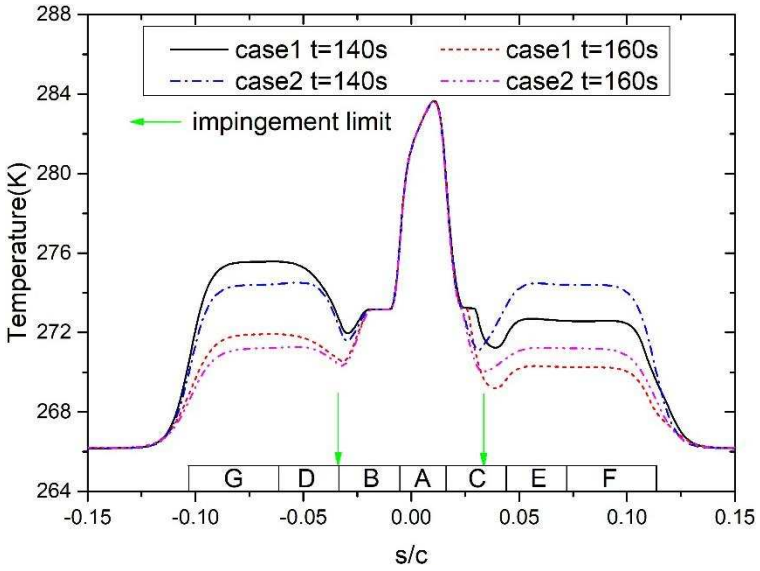

(a) Surface temperature distributions.

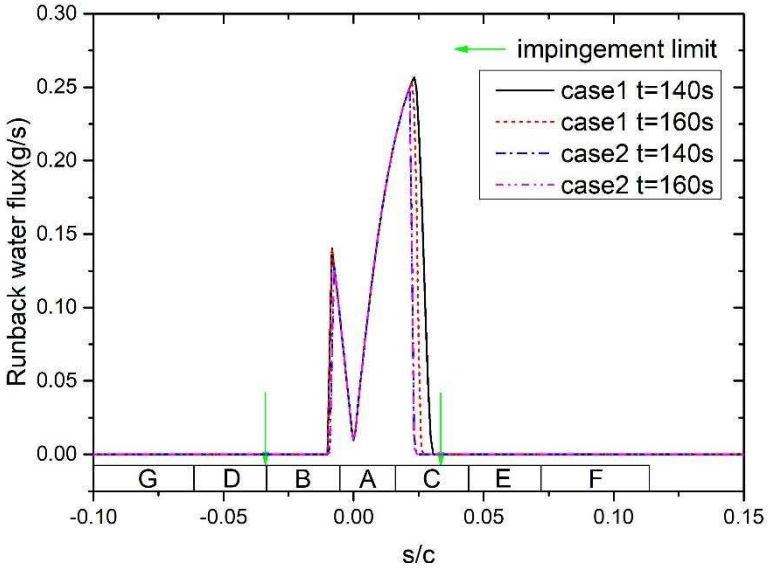

(b) Runback water flux distributions.

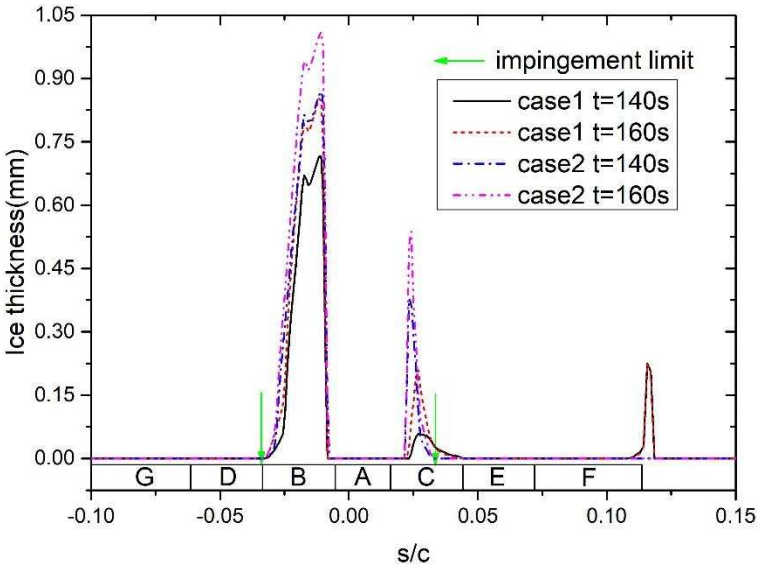

(c) Ice thickness distributions.

Figure 11. Results at different times in the re-freezing process.

Conclusions

In the present work, the mass and energy sources carried by the accumulated ice layer are successfully added into the unsteady thermodynamic model of the runback water. With redefinition of the freezing coefficient, the electro-thermal de-icing simulation are carried out by a temperature-based method, which couples the heat transfer between the runback water and the solid skin at each time step. The transient results of the NACA 0012 electro-thermal deicing system are compared with the literature data, and the temperature deviations are acceptable, verifying the unsteady temperature-based deicing model.

The simulation results also show that the established deicing model is slightly affected by the time step. Then, the heat and mass transfer characteristics are analyzed during the icing, ice melting and re-freezing processes in the transient deicing simulation,

and the main features are seen to be well modeled. In addition, it is found that the unsteady temperature distributions are greatly affected by the accumulated ice layer on the deicing surface, and the ice shedding effects will be studied and added into the deicing model in the subsequent research.

Funding

This work was supported by the National Natural Science Foundation of China (Grant No. 51806008 and No. 51206008).

References

1. Heinrich A, Ross R, Zumwalt G. Aircraft icing handbook. Volume 1. *Atlantic City International Airport*, NJ 08405: Department of Transportation, Federal Aviation Administration Technical Center, DOT/FAA/CT-88/8-1.

2. Cao Y, Tan W, Wu Z. Aircraft icing: An ongoing threat to aviation safety. *Aerospace Science and Technology*, 2018; 75: 353-385. DOI: 10.1016/j.ast.2017.12.028

3. Shinkafi A, Lawson C. Enhanced method of conceptual sizing of aircraft electro-thermal de-icing system. *International Journal of Aerospace and Mechanical Engineering*, 2014; 8(6): 1073-1080.

4. Bu XQ, Lin GP, Yu J, Shen XB, Hou PX. Numerical analysis of a swept wing hot air ice protection system. *Proceedings of the Institution of Mechanical Engineers, Part G: Journal of Aerospace Engineering, 2014;* 228(9): 1507-1518.

DOI: 10.1177/0954410013494515

5. Silva GAL, Silvares OM, Zerbini EJGJ. Numerical Simulation of Airfoil Thermal Anti-ice Operation, Part 2: Implementation and Results. *Journal of Aircraft* 2007; 44(2): 634-641. DOI: 10.2514/1.24922

6. Bennani L, Villedieu P, Salaun M, Trontin P. Numerical simulation and modeling of ice shedding: Process initiation. *Computers and Structures*, 2014; 142: 15-27. DOI: 10.1016/j.compstruc.2014.06.001

7. Pourbagian M, Habashi WG. Aero-thermal optimization of in-flight electro-thermal ice protection systems in transient de-icing mode. *International Journal of Heat and Fluid Flow* 2015; 54: 167-182. DOI: 10.1016/j.ijheatfluidflow.2015.05.012

8. Electro-thermal ice protection system for the B-787. *Aircraft Engineering and Aerospace Technology*, 2007; 9(6).

9. Reid T, Baruzzi GS, Aliaga C, Habashi WG. FENSAP-ICE: Application of unsteady CHT to de-icing simulations on a wing with inter-cycle ice formation. AIAA paper, no. 2010-7835, 2010.

10. Thomas SK, Cassoni RP, MacArthur CD. Aircraft anti-icing and de-icing techniques and modeling. *Journal of Aircraft*, 1996; 33(5): pp. 841-854. DOI: 10.2514/3.47027

11. J.R. Stallabrass, Thermal aspects of de-icer design, in: The International Helicopter Icing Conference, 1972.

12. Roelke RJ, Keith TG, Dewitt KJ, Wright WB. Efficient numerical simulation of a one-dimensional electrothermal deicer pad. *Journal of Aircraft*, 1988; 25(12): 1097-1101. DOI: 10.2514/3.45708

13. Yaslik AD, DeWitt KJ, Keith TG. Further developments in three-dimensional numerical simulation of electrothermal deicing systems. AIAA paper, no. 92-0528, 1992.

14. Huang JR, Keith TG, Dewitt KJ. Effect of curvature in the numerical simulation of an electrothermal de-icer pad. *Journal of Aircraft*, 1995; 32(1): 84-91.DOI: 10.2514/3.46687

15. Lei GL, Dong W, Zheng M, Guo ZQ, Liu YZ. Numerical investigation on heat transfer and melting process of ice with different porosities. *International Journal of Heat and Mass Transfer*, 2017; 107: 934-944.

DOI: 10.1016/j.ijheatmasstransfer.2016.11.004

16. Wright WB, Keith TGJ, Dewitt KJ. Numerical analysis of a thermal deicer. AIAA paper, no. 92-0527, 1992.

17. Wright WB, Al-Khalil KM, Miller DR. Validation of NASA thermal ice protection computer codes: Part 2: The validation of LEWICE/Thermal. AIAA paper, no. 97-0050, 1997.

18. Myers TG, Charpin JPF. A mathematical model for atmospheric ice accretion and water flow on a cold surface. *International Journal of Heat and Mass Transfer*, 2004; 47: 5483-5500. DOI: 10.1016/j.ijheatmasstransfer.2004.06.037

19. Harireche O, Verdin P, Thompson CP, Hammond DW. Explicit finite volume modeling of aircraft anti-icing and de-icing. *Journal of Aircraft*, 2008; 45(6): 1924-1936. DOI: 10.2514/1.34855

20. Reid T, Baruzzi GS, Habashi WG. FENSAP-ICE: unsteady conjugate heat transfer simulation of electrothermal de-icing. *Journal of Aircraft*, 2012; 49(4): 1101-1109.

DOI: 10.2514/1.C031607

21. Ding L, Chang S, Yang S, Leng M. Study on heating strategies of nose cone electrothermal anti-icing. *Journal of Aircraft*, 2018; 55(3): 1310-1314.

DOI: 10.2514/1.C034639

22. Mu ZD, Lin GP, Shen XB, Bu XQ, and Zhou Y. Numerical Simulation of Unsteady Conjugate Heat Transfer of Electrothermal Deicing Process. *International Journal of Aerospace Engineering* 2018. 2018: 1-16. DOI: 10.1155/2018/5362541.

23. *ANSYS FLUENT User's Guide*. release 18.0. ANSYS, Inc; 2018.

24. Shen X, Lin G, Yang S, Wang H. Eulerian method for droplets impingement calculation. Proceedings of 48th SAFE Symposium, 2011.

25. Silva GAL, Silvares OM, Zerbini EJGJ. Numerical Simulation of Airfoil Thermal Anti-ice Operation, Part 1: Mathematical Modelling. *Journal of Aircraft* 2007; 44(2):627-633. DOI: 10.2514/1.544.

26. Messinger BL. Equilibrium temperature of an unheated icing surface as a function of airspeed. *Journal of the Aeronautical Sciences* 2012; 20(1): 29-42. DOI: 10.2514/8.2520.

27. Bu XQ, Lin GP, Yu G, Yang SH, Song X. Numerical simulation of an airfoil electrothermal anti-icing system. *Proceedings of the Institution of Mechanical Engineers - Part G: Journal of Aerospace Engineering,* 2013; 227(10): 1608-1622.
DOI: 10.1177/0954410012463525.

28. Domingos RH, Papadakis M, Zamora AO. Computational Methodology for Bleed Air Ice Protection System Parametric Analysis. AIAA paper, no. 2010-7834, 2010.

29. Wright WB. User manual for the NASA Glenn ice accretion code LEWICE version 2.2.2. NASA-CR-2002-211793, 2002.

30. Shen X, Liu X, Lin G, Bu X, Wen D. Effects of Anisotropic Composite Skin on Electro-thermal Anti-icing System. *Proceedings of the Institution of Mechanical Engineers - Part G: Journal of Aerospace Engineering*, 2019; 0(0): 1-11.
DOI: 10.1177/0954410019845980.